CrossMark

Three-dimensional flow field around and downstream of a subscale model rotating vertical axis wind turbine

Kevin J. Ryan[1] · Filippo Coletti[2] · Christopher J. Elkins[1] · John O. Dabiri[3] · John K. Eaton[1]

Abstract Three-dimensional, three-component mean velocity fields have been measured around and downstream of a scale model vertical axis wind turbine (VAWT) operated at tip speed ratios (TSRs) of 1.25 and 2.5, in addition to a non-rotating case. The five-bladed turbine model has an aspect ratio (height/diameter) of 1 and is operated in a water tunnel at a Reynolds number based on turbine diameter of 11,600. Velocity fields are acquired using magnetic resonance velocimetry (MRV) at an isotropic resolution of 1/50 of the turbine diameter. Mean flow reversal is observed immediately behind the turbine for cases with rotation. The turbine wake is highly three-dimensional and asymmetric throughout the investigated region, which extends up to 7 diameters downstream. A vortex pair, generated at the upwind-turning side of the turbine, plays a dominant role in wake dynamics by entraining faster fluid from the freestream and aiding in wake recovery. The higher TSR case shows a larger region of reverse flow and greater asymmetry in the near wake of the turbine, but faster wake recovery due to the increase in vortex pair strength with increasing TSR. The present measurement technique also provides detailed information about flow in the vicinity of the turbine blades and within the turbine rotor. The details of the flow field around VAWTs and in their wakes can inform the design of high-density VAWT wind farms, where wake interaction between turbines is a principal consideration.

1 Introduction

One well-known obstacle facing most sources of renewable energy is the significantly decreased energy density with respect to fossil fuels. Energy density of wind power is further penalized by the need for wind turbines to be spaced far enough apart to not interfere with one another. Conventional horizontal axis wind turbines (HAWTs) must be spaced far apart [3–5 turbine diameters in the cross-wind direction, 6–10 diameters in the downwind direction (Sørensen 2004; Hau 2005)]. This energy density imbalance requires that wind farms have a large land area to generate significant power.

Vertical axis wind turbines (VAWTs) have promise in increasing the energy density of wind power beyond HAWTs. The swept area of a VAWT can be increased independently of its footprint by extending the rotor blade height, thereby increasing power extraction for the same wind farm footprint. Individual VAWT rotors can also be more closely packed than HAWTs. A recent study showed that the distance behind the turbine required to regain 95 % of the upwind velocity was 15 diameters for a traditional HAWT, but only 4 for a straight-bladed VAWT (Dabiri 2011). It has also been hypothesized that optimal layouts of VAWT arrays can benefit from constructive aerodynamic interactions of neighboring turbines (Whittlesey et al. 2010). Following these observations, it was argued that the power density of optimal VAWT arrays could be an order of magnitude higher than present HAWT farms (Dabiri 2011).

✉ Kevin J. Ryan
kjryan@stanford.edu

[1] Flow Physics and Computational Engineering, Department of Mechanical Engineering, Stanford University, Stanford, CA 94305, USA

[2] Department of Aerospace Engineering and Mechanics, University of Minnesota, Minneapolis, MN 55455, USA

[3] Departments of Civil and Environmental Engineering and Mechanical Engineering, Stanford University, Stanford, CA 94305, USA

The above observations are based on limited experimental investigations of the velocity fields around VAWTs. Most of these measurements have been confined to single planes upstream of the rotor or in the turbine wake (Kinzel et al. 2012; Brochier et al. 1986; Dixon et al. 2008; Battisti et al. 2011; Ferreira et al. 2006, 2010; Hofemann et al. 2008). To fully understand the highly complex flow field around a spinning VAWT, three-dimensional, volumetric velocity measurements are required.

Three-dimensional high-fidelity simulations of large VAWT arrays are expected to be prohibitively expensive in the foreseeable future. For flow around a single turbine, Bazilevs et al. (2014) performed a simulation including fluid-structure interaction between the turbine and oncoming fluid flow. They found good agreement with experimentally measured torque and investigated turbine self-start from various initial rotation rates. Several models have been proposed to simplify the calculation of flow around a single VAWT. Shamsoddin and Porté-Agel (2014) performed a large eddy simulation of the experimental setup of Brochier et al. (1986), using the actuator swept-surface model (ASSM) and actuator line model (ALM) to represent the VAWT. Both of these models substantially simplify the force field applied by the blades. Other studies, such as those by Rajagopalan and Fanucci (1985) and Fortunato et al. (1995), have assumed that the turbine has similar aerodynamics to a porous spinning cylinder; however, validation of this technique was only provided against other computational results. Howell et al. (2010) compared 2D and 3D simulations of a VAWT with experimental data and showed that from the point of view of the turbine performance coefficient, the 2D simulations were unable to match experimentally measured values as well as the 3D cases. They proposed that the difference could be explained by the fact that the 2D case does not allow for the tip vortices that are present in the real turbine and are captured by the 3D simulation. However, they still lack the measured velocity fields necessary to validate their 3D simulations.

Many models used to simulate VAWTs, such as the blade element momentum (BEM), ALM, ASSM, and double multiple streamtube (DMS) models, represent the effect of the turbine on the flow field by localized forces included in the Navier–Stokes equations. To reduce computational cost, the motion of the turbine is not solved for in the simulation, but rather the location of applied forcing is moved throughout the domain using the prescribed tip speed ratio (TSR). Forcing is typically represented as the lift and drag forces induced by the blade, which are found by table lookups based on the angle of attack (AOA). Determination of a blade's AOA requires local velocity vectors, which can differ significantly from the unperturbed bulk velocity due to the rotation of the turbine. Despite this, studies by Dixon et al. (2008) and Laneville and Vittecoq (1986) used the bulk velocity to find the geometric AOA in discussions of dynamic stall of turbine blades. Due to the difficulty of performing measurements near the blades, very few reported studies include experimental measurements of the actual AOA. Laneville and Vittecoq (1986) measured lift and drag forces on individual blades as a function of their azimuthal position during turbine rotation and found nonzero lift and drag for an airfoil nominally at zero AOA, suggesting a different actual AOA than the geometric definition. Castelli et al. (2011) performed a 2D CFD study using three zonal meshes, the finest of which resolved flow around individual blades. They reported the difference between the geometric and local AOA for different TSRs, noting a decrease in AOA magnitude for increasing TSR. Experimental measurements of AOA at the resolutions they report are still lacking.

In the present work, the full three-component mean velocity field around and downstream of a scale model of a rotating VAWT is measured using magnetic resonance velocimetry (MRV). Three TSRs, including a stationary baseline case, are investigated and compared. In addition to illustrating the near turbine flow field and downstream wake dynamics, the results can inform low-order models and provide insight into optimal wind farm design.

2 Experimental methodology

2.1 Setup and flow regimes

The wind turbine model is set up in a water tunnel assembled from components fabricated with stereolithography and an acrylic test section. The total length is 1730 mm (Fig. 1). Three diffusing sections expand the 38-mm-diameter circular inlet to a 196 mm by 196 mm square cross-section. Ten grids and a honeycomb are placed throughout the diffusers to prevent separation and remove large-scale secondary flows. After the diffusing section, a contraction of area ratio 1.78:1 serves to homogenize the velocity of the flow entering the 196 mm by 110 mm test section. Due to the spatial constraints of operating the water tunnel inside the bore of a medical-grade MRI magnet, only a relatively small contraction ratio is allowable. The boundary layer thickness at the most upstream measurement location (i.e., 1.4 turbine diameters upstream of the turbine axis) is approximately one half of a turbine diameter, but the precise determination of the boundary layer thickness is complicated by the presence of the turbine affecting the incoming velocity field at this station. A more relevant measure is the change in incoming velocity across the height of the turbine model, which varies 15 % in the present study.
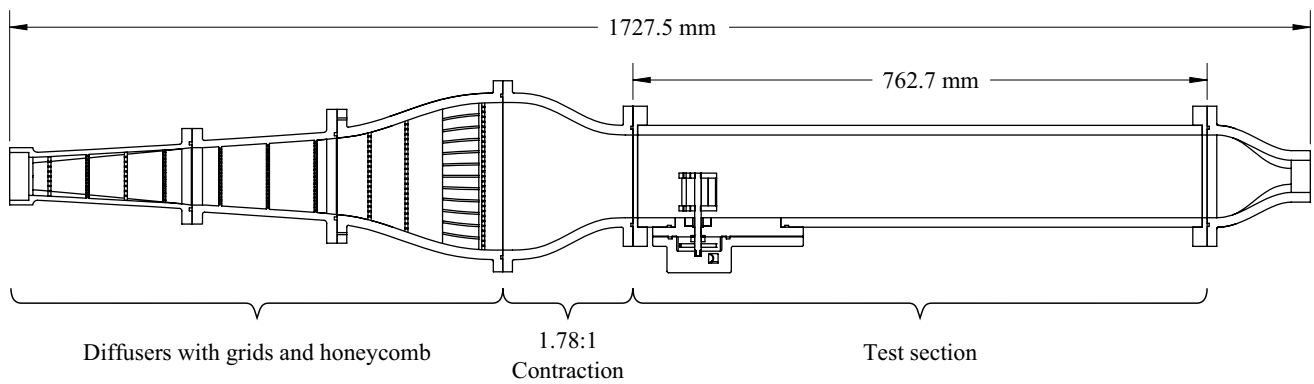
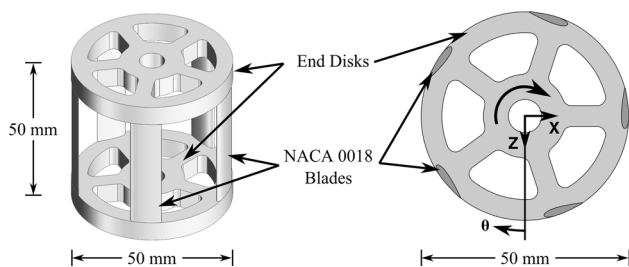**Fig. 1** Schematic of water tunnel

Diffusers with grids and honeycomb | 1.78:1 Contraction | Test section

Fig. 2 Vertical axis wind turbine model with aspect ratio 1. *Top–down view* defines azimuthal coordinate θ in relation to X and Z

Fig. 3 Schematic of hydraulic spinning mechanism with paddle-wheel and gearing. Gear ratio is changed to achieve desired TSR. Paddlewheel housing surrounds gearing and paddlewheel and is omitted for clarity

This matches the 15 % change observed by Kinzel et al. (2012) in at-scale measurements. The acrylic test section is 760 mm long and smoothly connects to the 38-mm-diameter outlet.

The five-bladed turbine model (Fig. 2) consists of NACA 0018 airfoils of 1.8 mm maximum thickness supported between two end disks. The last 0.3 mm of the blade chord length is truncated for manufacturability. Both height H and diameter D of the model are 50 mm, and the model is fabricated as a single piece using stereolithography. The design of the turbine is influenced by commercially available VAWTs having five blades and near-unity aspect ratio. The model is supported by a 9.5 mm PVC post, which rotates in bearings embedded in the wall of the test section (Fig. 3). The bottom of the turbine is 0.2D above the test section wall.

The scaled turbine model does not extract enough torque from the fluid flow to spin freely, due to the added friction in the support bearings and seals in the test section wall. A custom drive mechanism is used to rotate the turbine at the desired speed. The entirely nonmetallic and MR-safe hydraulic drive consists of a paddlewheel and housing located beneath the turbine (Fig. 3) through which a secondary water circuit flows. Torque is transferred from the paddlewheel to the turbine model through a set of gears. A laser tachometry system consisting of a Thorlabs CPS180
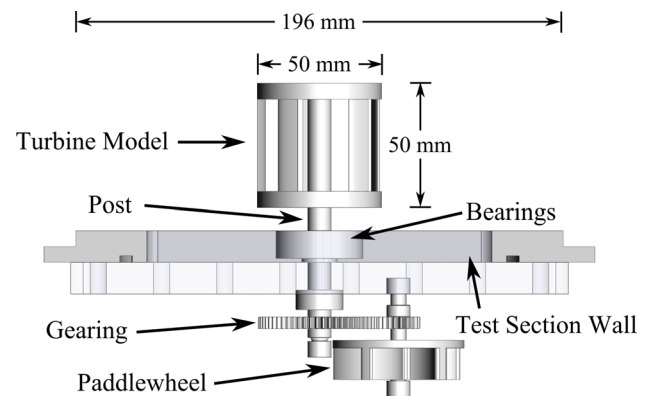
laser diode and DET36A photodetector measures the turbine rotational speed. The laser beam passes through the turbine rotor where it is interrupted by the passing of the blades. A Fourier analysis of the acquired signal provides the blade passing frequency. Throughout the experiment, the secondary flowrate through the paddlewheel housing is adjusted to maintain the desired turbine rotational speed based on the present blade passing frequency.

An aqueous solution of copper sulfate at a concentration of 0.06 mol/L (added to increase MRV signal) is used as the working fluid. The closed-loop flow system for the main water tunnel includes a holding tank, pumps, and 38-mm-diameter plastic hoses. Two Berkeley BPDH10-L electric pumps drive the main flow, which is measured by a Signet Instruments 515 Paddlewheel Flow Sensor. A separate tank and Little Giant TE-6-MD-HC pump provide flow to the hydraulic drive system through 25-mm-diameter plastic hoses. The flowrate through the tunnel is maintained at 270 L/min, equivalent to a bulk velocity of $U_0 = 0.21$ m/s in the tunnel test section. The Reynolds numbers based

Table 1 Nominal geometric and flow parameters

Parameter	Value
D (mm)	50
H (mm)	50
D_H (mm)	141
U_0 (m/s)	0.21
Re_{bulk}	32,700
Re_D	11,600
λ	0, 1.25, 2.5

on the turbine diameter D and channel hydraulic diameter D_H are 11,600 and 32,700, respectively. The tip speed ratio λ is defined by the equation:

$$\lambda = \frac{\Omega D/2}{U_0} \tag{1}$$

where Ω is the rotation frequency. The three TSRs chosen for this study, $\lambda = 0$, 1.25, and 2.5, reflect the operating range of commercial turbines as well as the values commonly studied in the literature. Kinzel et al. (2012) studied full-scale VAWTs operating at $\lambda = 2.3$, and Battisti et al. (2011) measured wake profiles behind VAWTs at $\lambda = 1.6$ and $\lambda = 2.5$. Simulations of a five-bladed VAWT by Raciti Castelli et al. (2012) investigated changes in power coefficient over $1.44 < \lambda < 3.3$ and found a maximum at $\lambda = 2.0$. The main geometrical and flow parameters of the present study are given in Table 1.

2.2 Magnetic resonance velocimetry

Three-dimensional, three-component velocity fields are obtained using magnetic resonance velocimetry (MRV) described by Elkins et al. (2003). Measurement of velocity is possible due to the sensitivity of the phase of the acquired MR signal to motion. Pelc et al. (1994) detail the data acquisition procedure for such measurements. Experiments are performed using a 3.0 Tesla General Electric whole body scanner at the Richard M. Lucas Center for Imaging at Stanford University. Three-component velocity vectors are acquired on an isotropic 1 mm Cartesian grid spanning the entire channel volume.

The MRV technique acquires velocities in Fourier space in terms of spatial frequency components. Individual acquisitions last between 7 and 10 min. After the acquisition, the velocity field is reconstructed from the Fourier space data to produce a velocity field. Measurements are not phase-locked to turbine rotation, but instead, the reconstruction is the velocity field time-averaged over the acquisition period. For the slower case with rotation, $\lambda = 1.25$, the period of successive blade passings is 120 ms. More than 4000 blade passing periods occur over the course of a single

acquisition; therefore, the reconstructed velocity field well represents the time-averaged field. To increase data quality and reduce measurement noise, six to eight acquisitions are averaged for each region of interest. Comparisons of individual data acquisitions show excellent agreement and indicate that the mean flow features are repeatable.

Two regions of interest are combined for each investigated TSR, resulting in a full data set extending over $-1.4 < X/D < 6.9$. The transition between the two regions of interest occurs in a region of overlap between $2 < X/D < 4$ and varies between cases. Excluding the region of overlap, each data set contains roughly 8.9 million velocity vectors on a Cartesian grid.

2.3 Experimental uncertainty

The range of measurable velocities in MRV depends on a parameter known as the velocity encoding, Venc. This value represents the maximum velocity that can be measured free of aliasing and must be greater than all velocities within the flow. The prescribed Venc also influences the MRV uncertainty, which can be calculated using (Pelc et al. 1994)

$$\delta_v = \frac{\sqrt{2}}{\pi} \frac{\text{Venc}}{\text{SNR}} \tag{2}$$

where the signal-to-noise ratio SNR is the ratio of MRV signal magnitude within the channel region to that in the solid walls. The upstream and downstream regions of interest have an uncertainty of 6.2 and 4.3 % of the bulk velocity U_0, respectively.

The main flow rate is continuously monitored over each acquisition. Fluctuations in the flowmeter reading result in an uncertainty in Reynolds number below 2 %. The photodetector output is sampled for 4 s at 400 Hz, and a fast Fourier transform is performed on the acquired signal to provide real time feedback of the turbine rotation rate. The rotation rate over each 4 s sampling period is recorded throughout the 7–10-min acquisition. Statistical analysis of the measured turbine rotation rate over the acquisition period provides an uncertainty in the mean rotation rate of 4.8 %, at 95 % confidence. Combined with the uncertainty in Reynolds number, the uncertainty in turbine TSR is 5.1 %, also at 95 % confidence.

2.4 Experimental limitations

The present study makes use of a simplified model of a realistic VAWT and its operating conditions. Although the Reynolds number is 10 to 100 times smaller than full-scale turbines, which operate over $10^5 < Re_D < 10^6$, it is high enough to create a fully turbulent wake behind the turbine. The flow in the VAWT near wake is characterized

by massive separation, which is largely influenced by inviscid dynamics. Therefore, although a quantitative comparison with full-scale installations is precluded, the reported trends and features of the wake are expected to apply qualitatively at higher Reynolds numbers.

Subscale Reynolds numbers are commonly found in the literature, as a consequence of performing measurements on scaled-down turbine models. Reynolds numbers span the regime of the present study ($Re_D = 1.2 \times 10^4$): Brochier et al. (1986) studied a turbine at $Re_D = 1.0 \times 10^4$, Araya and Dabiri (2015) performed measurements over the range $Re_D = 2.4 \times 10^4$–8.4×10^4, and Rolin and Porté-Agel (2015) looked at a rotor with $Re_D = 4.9 \times 10^4$. Bachant and Wosnik (2014) assessed the Reynolds number dependence of the wake behind a three-bladed VAWT model of aspect ratio 1, operated at $\lambda = 1.9$. Over a range of $Re_D = 3.0 \times 10^5$–1.4×10^6, they found excellent agreement of turbulence intensity and Reynolds shear stress in the turbine wake, with only minor deviations at the lowest Reynolds number. More relevant to the present study, they observed nearly identical streamwise time-averaged velocity over this range of Reynolds numbers. The invariability of time-averaged velocity measurements in the wake suggests that the conclusions drawn from the time-averaged mean flow of the present work would be applicable to higher Reynolds numbers.

Although the MRV measurement technique does not provide a quantitative measurement of the turbulence in the test section, studies performed on other test sections with similar inlet flow conditioning show freestream turbulence intensities of <2 % for streamwise and wall-normal components (Coletti et al. 2013). VAWTs operating in atmospheric conditions would experience higher levels of freestream turbulence, increasing mixing in the wake and decreasing wake recovery distance.

The use of a hydraulic drive system to spin the turbine adds energy to the flow, preventing the analysis of turbine performance from an energy transfer standpoint. The turbine is therefore operated in kinematic, as opposed to dynamic, similarity. With the present experimental setup, it is challenging to determine how much of the energy from the paddlewheel spinning mechanism is lost in the bearings and seals, and how much is added to the fluid through the turbine. Howell et al. (2010) calculated an estimate of the bearing loss and found that it could vary from 30 to 70 % of the total extracted torque by the turbine. While their experimental setup differs from the one in the present study in many ways, this suggests that much of the energy provided to spin the turbine model is used to overcome bearing losses. Araya and Dabiri (2015) compared measurements in the near wake of flow-driven and motor-driven VAWT models using PIV on the turbine mid-height plane. They found nearly identical streamwise and lateral

mean velocity profiles, lateral velocity fluctuation power spectra, shaft torque, and circulation in the wake for flow-driven and motor-driven VAWT models over a TSR range of $1.19 < \lambda < 1.70$. They concluded that the kinematics of the spinning turbine, not the method by which it is set in motion, is the dominant factor in correctly capturing the wake dynamics. The use of a driven turbine in the present study is supported by these findings.

With the restricted size of the test section, the solid turbine model creates a significant blockage to the incoming flow, with a blockage ratio of 12 % based on the total frontal area or 8.4 % considering turbine solidity of 70 %. Blockage ratios of 10–25 % are common in similar studies. Battisti et al. (2011) measured the velocity profiles behind a VAWT in a wind tunnel with a 10 % blockage ratio and in an open configuration with low blockage and found qualitative similarity between the two. In the vicinity of the turbine, the blockage forces the flow to accelerate, creating higher velocities than would occur for a turbine operating in the open atmosphere. Much of the turbine's solidity comes from the end disk and post support structures, which could not be scaled to the same degree as the airfoils. The effects of these structures are examined in the section on 3D wake. The proximity of the bottom wall of the test section to the turbine model, which is closer than would occur in a VAWT in an operational installation, is also addressed in relation to wake development.

Correction methods for the blockage effect on VAWTs in confined test sections have not been clearly identified in the literature. Dossena et al. (2015) propose a correction factor relating the approach velocities of confined and unconfined turbines, found by equating experimentally measured thrust for the two configurations. However, it is not evident that their findings are generalizable to different turbine models, and would only change the reported approach velocity U_0 in the present work. Using their estimates, TSRs 1.25 and 2.5 have a correction of 4 and 7 %, respectively, which is close to the measurement uncertainty of the present study. One of the few studies by Roy and Saha (2014) shows that the effects of blockage up to 10 % are almost negligible (although dependent on TSR). This is in general agreement with recent experimental and numerical studies of blockage effects on HAWTs (McTavish et al. 2014). While the present blockage ratio of 12 % will certainly produce quantitative differences, we believe the fundamental wake dynamics, which is the object of our attention, will not be qualitatively changed.

The present study addresses a low aspect ratio turbine, and this has major consequences on the wake three-dimensionality and general evolution. While this aspect ratio is representative of some existing VAWTs, we remark that more elongated designs will lead to qualitatively different behavior of the wake.

Because of the several limitations of the present study, the reported results and conclusions are not expected to be quantitatively applicable to full-scale VAWTs. Our goal is rather to explore qualitative aspects of the 3D vortical flow in the wake of a vertical axis turbine. While we expect this to lead to insightful considerations on the general aspects of similar flows, the degree of applicability of the results to actual VAWTs shall be verified by careful comparison with field measurements. Future research is warranted in this direction.

3 Results

This section presents the time-averaged velocity fields obtained for the three cases, $\lambda = 0$, 1.25, and 2.5. The results are normalized by the turbine diameter D and the bulk velocity U_0. X, Y, and Z indicate streamwise, wall-normal, and lateral directions, respectively, and the origin is located at the intersection of the turbine axis with the bottom wall of the test section. The turbine rotates clockwise for an observer looking down onto it. The turbine is represented in the same angular position in each plot. This is the actual position imposed during the stationary ($\lambda = 0$) measurements.

3.1 Near wake

3.1.1 Mid-height velocity vectors

Figure 4 shows in-plane vectors of time-averaged velocity taken from a wall-normal plane at the turbine mid-height ($Y/D = 0.7$) for the $\lambda = 0$ and $\lambda = 2.5$ cases (the latter being qualitatively similar to the $\lambda = 1.25$ case). At this location, wall-normal velocities are negligible (i.e., 6 % or less of the average in-plane velocity magnitude) and the flow can be well visualized as two-dimensional. Velocity vectors are shown at one quarter the resolution of the acquired data, which has 50 points across the diameter of the turbine, and nearly 100,000 points within the full turbine volume. At this resolution, individual mean flow structures within the envelope of the turbine are clearly visible. For the stationary turbine, the two most upstream blades show large regions of stall and recirculation in their wake, while the most downstream blade sits in the wake of the post, which also has regions of flow reversal. Much of the flow approaching the turbine is allowed to pass through the open volume within the model.

The flow within the turbine changes significantly with the addition of rotation, with the majority of velocity vectors following the clockwise rotation of the turbine. The flow at the most downstream extent of the turbine is purely in the lateral direction, and moving clockwise from this location the predominant velocities are directed upstream, against the imposed incoming flow. For blades passing through the bottom left corner of the turbine, the flows seen by the interior and exterior surfaces are inconsistent in both magnitude and direction. This will be an important point in the discussion of angle of attack to follow. Individual wakes behind turbine blades are no longer visible in the time-averaged velocity field, but at least two distinct recirculation regions can be seen immediately downstream of the post.
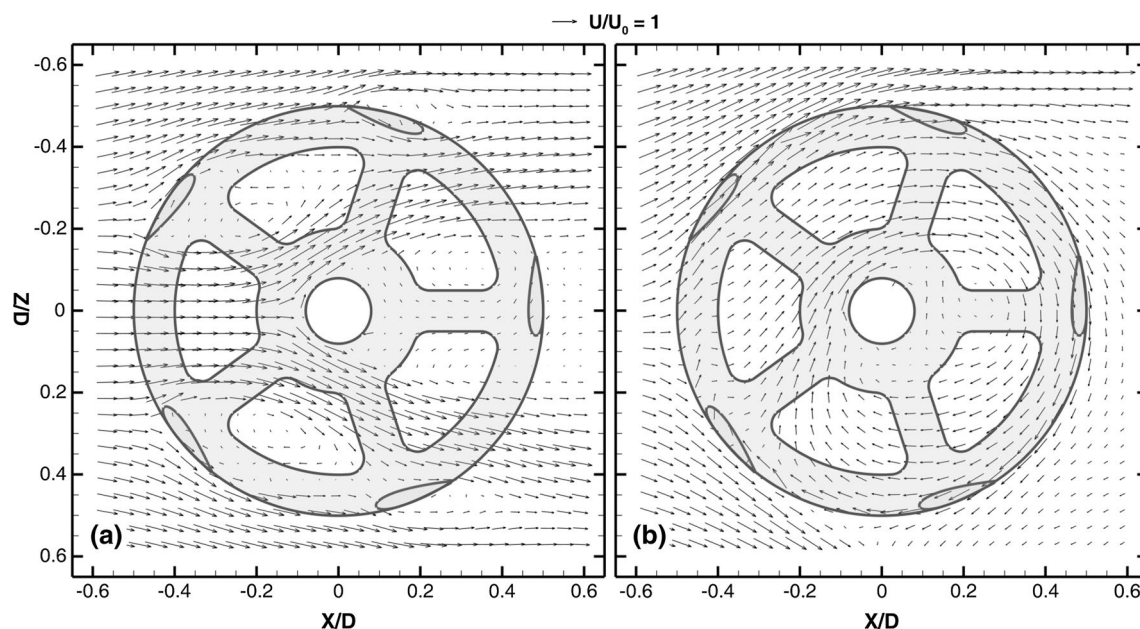

Fig. 4 In-plane velocity vectors at the turbine mid-height, $Y/D = 0.7$, for $\lambda = 0$ (**a**) and $\lambda = 2.5$ (**b**). Turbine is viewed from above, with flow entering from the *left*
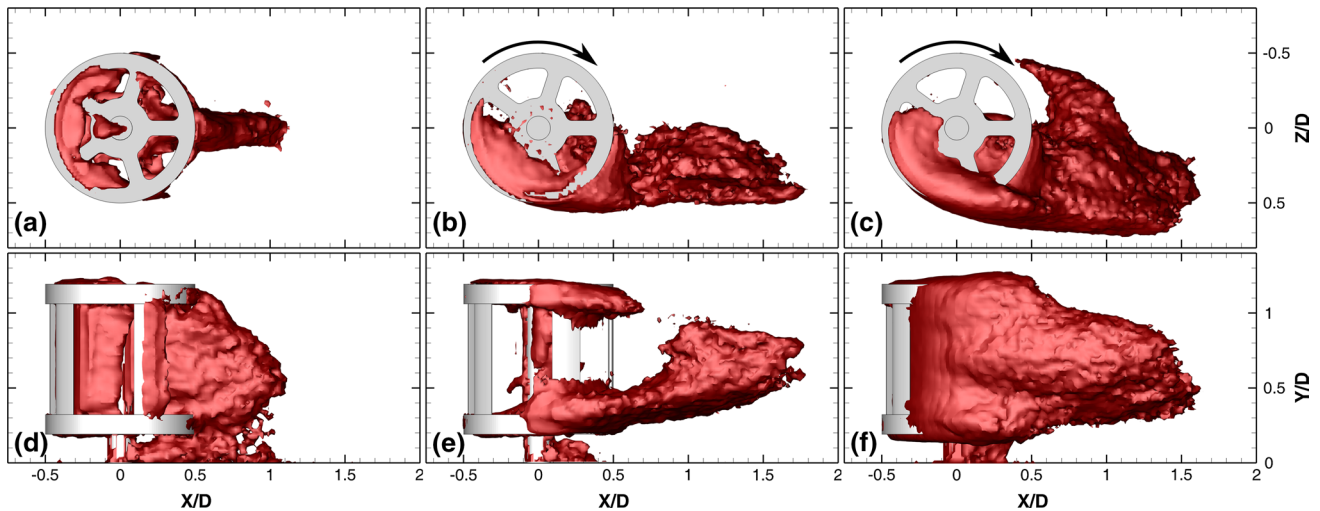
Fig. 5 Isosurfaces of reverse flow in the vicinity of the turbine, showing *top* and *side* views of the turbine for $\lambda = 0$ (**a**, **d**), $\lambda = 1.25$ (**b**, **e**), and $\lambda = 2.5$ (**c**, **f**). Fluid contained within the isosurface has $U/U_0 \leq 0$. The *arrows* in (**b**, **c**) indicate the direction of rotation of the turbine for the cases with rotation. The side of the turbine closest to the viewer in (**e**, **f**) is moving upstream (*left*) against the incoming flow

Compared to the stationary case, less fluid passes through the volume of the turbine, with more of the incoming flow deflected around the turbine in the lateral direction.

3.1.2 3D wake

Regions where the streamwise velocity component is directed upstream can be seen in Fig. 4. These reverse flow regions are visualized by 3D isosurfaces enclosing $U/U_0 \leq 0$ in Fig. 5. For the stationary case (Fig. 5a, d), the reverse flow behind the turbine consists of the individual wakes of the turbine blades and center post. When the turbine is in rotation, wakes of individual components are no longer visible, but a coherent volume of reverse flow occurs due to the motion of the rotor on the upwind-turning side of the turbine ($\theta < 90°$, $\theta > 270°$, see Fig. 2). At $\lambda = 1.25$ (Fig. 5b, e), the reverse flow volume is small and is confined to regions near the end disks. Fluid at these locations is always in contact with a moving solid surface and is therefore more likely to be propelled upstream. The intermittent presence of blades in the middle of the turbine is not sufficient to cause reverse flow at the lower TSR. For the higher TSR ($\lambda = 2.5$, Fig. 5c, f), faster moving blades produce reverse flow that spans the entire upwind-turning side of the turbine. The size and magnitude of the reverse flow regions are examined by measuring the volume, maximum reverse flow velocity, and mean reverse flow velocity for points exterior to the turbine rotor with $U/U_0 \leq 0$. The results are shown in Table 2. The $\lambda = 0$ and $\lambda = 1.25$ cases have similar maximum and mean reverse flow velocities, despite the doubling in volume of the reverse flow region for the rotating turbine. The reverse flow volume and

Table 2 Volume and velocity statistics of the reverse flow region

	$\lambda = 0$	$\lambda = 1.25$	$\lambda = 2.5$
Reverse flow volume/D^3	0.09	0.18	0.49
Max reverse flow/U_0	-0.26	-0.29	-0.61
Mean reverse flow/U_0	-0.08	-0.06	-0.14

Measurements were restricted to data outside of the turbine rotor

velocity metrics more than double as the TSR is increased from 1.25 to 2.5.

3.1.3 Transverse planes

Near wake development is examined through secondary flow features on cross-sections perpendicular to the main flow direction (Fig. 6). For $\lambda = 0$ (Fig. 6a, b), the wake at $X/D = 1.3$ is approximately symmetric and is largely contained within the projected area of the turbine. Relatively weak secondary flows direct freestream fluid behind the turbine, making up for the initial blockage seen by the incoming flow.

The rotation induces two tip vortices that originate from the upwind-turning side of the turbine (Fig. 6c, e). These vortices entrain higher velocity fluid from above and around the turbine and mix it with the slow flow in the wake, quickening wake recovery. The effect of the bottom vortex is damped by the bottom wall of the test section, creating a strong top–bottom asymmetry in the wake at $X/D = 1.3$. The left–right asymmetry in vortex structure is reflected in the wake development, where the flow between the single vortex pair shifts the wake toward the positive Z direction.
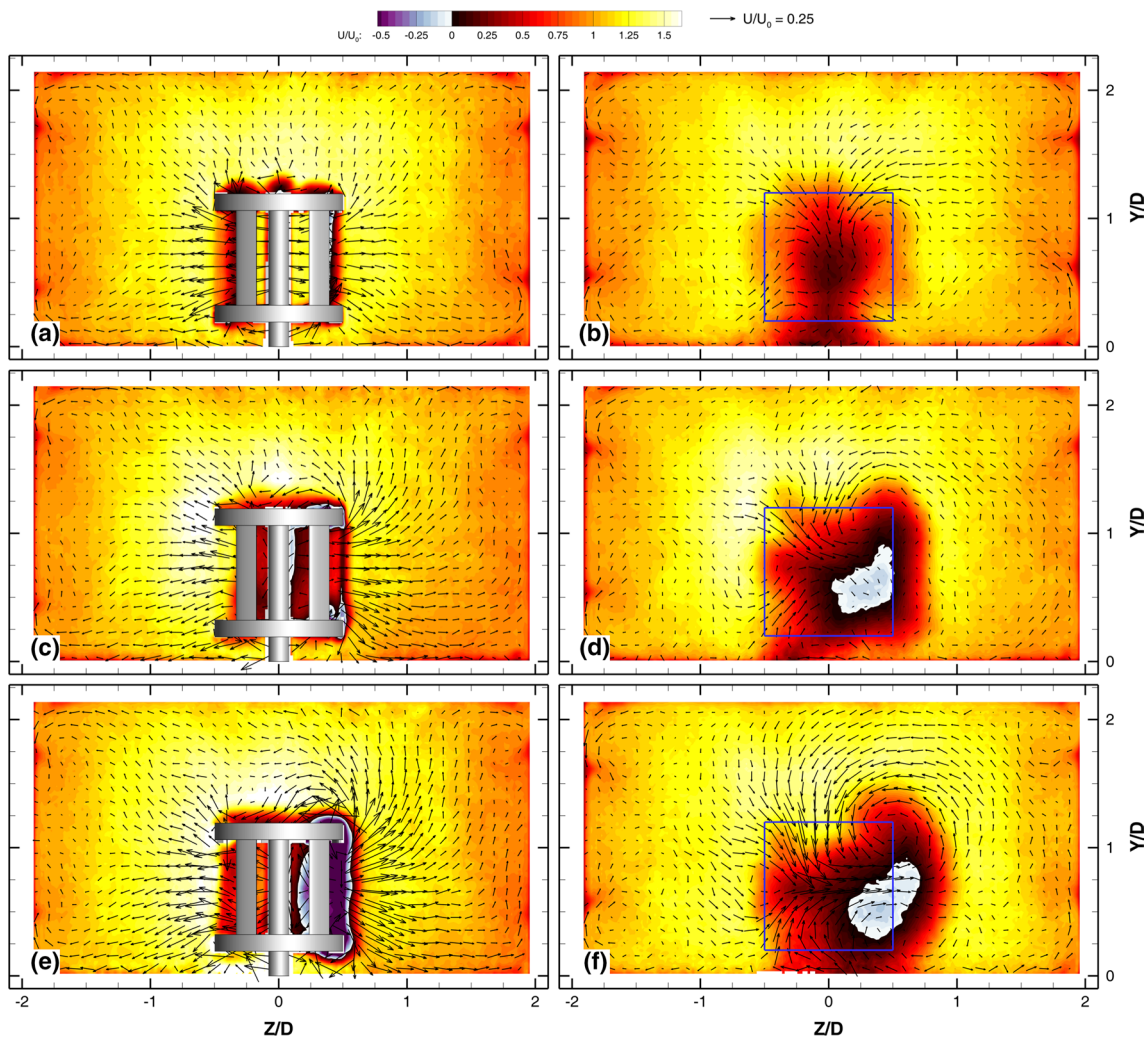
Fig. 6 Transverse slices, looking downstream, showing *color contours* of streamwise velocity with in-plane velocity vectors for $\lambda = 0$ (**a**, **b**), $\lambda = 1.25$ (**c**, **d**), and $\lambda = 2.5$ (**e**, **f**). For each tip speed ratio, two locations are shown, $X/D = 0$ (**a**, **c**, **e**) and $X/D = 1.3$ (**b**, **d**, **f**). The *white-to-purple* contours indicate regions of mean flow reversal, $U/U_0 < 0$. Only 4 % of measured velocity vectors are shown for clarity. At $X/D = 1.3$, the projection of the turbine is shown as a *blue outline*

Vortex strength increases with TSR, producing greater wake asymmetries at the downstream location. For $\lambda = 1.25$, the region of reverse flow is contained within the projected area of the turbine, whereas the wake and reverse flow region for $\lambda = 2.5$ extend beyond the turbine projection. The increasing strength of the vortex pair with TSR will also be shown to shorten the wake recovery distance in following sections.

To better visualize the vortex pair, isosurfaces of streamwise vorticity at a non-dimensional value of $\omega_X = \pm 3U_0/D$ are shown in Fig. 7. The stationary turbine in Fig. 7a shows pairs of vortices originating from the corners of the turbine, symmetric about the $Z = 0$ plane. With rotation, the lateral velocity imparted to the fluid by the end disks creates regions of strong shear on the top and bottom of the turbine. Above the turbine, this results in positive vorticity at the upstream side and negative on the downstream side, with vortex directionality reversed

below the turbine. Downstream, the shear-dominated vorticity above the turbine rolls up into the coherent vortices seen in Fig. 6. The swirling motion beneath the turbine is damped by the proximity of the bottom wall of the channel and the momentum deficit in the boundary layer. The vorticity at the top of the turbine is less restricted and continues as a coherent vortex further downstream. With increasing TSR, the strength and longevity of this vortex increase, indicated by the size and streamwise extent of the vorticity isosurfaces.

3.2 Wake development

3.2.1 Streamwise planes

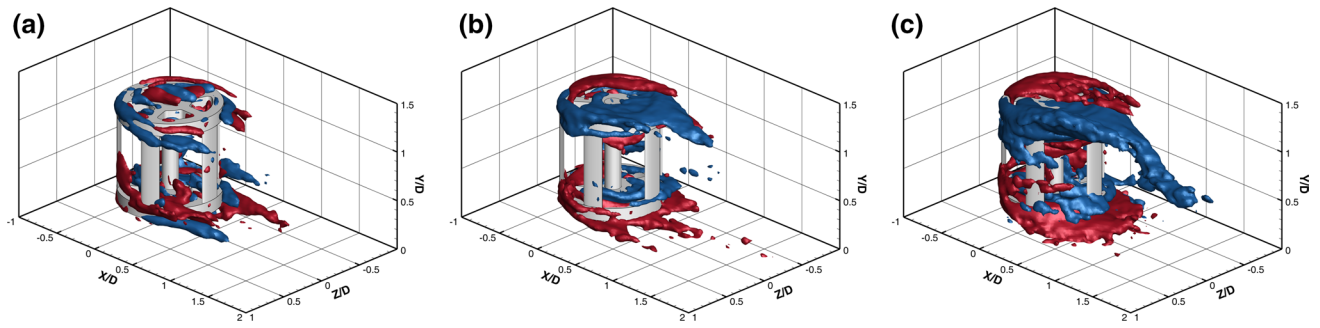Streamwise velocity contours along the $Z = 0$ symmetry plane are shown in Fig. 8. Flow accelerates in a *vena*

Fig. 7 3D isosurfaces of streamwise vorticity at $\omega_X = \pm 3U_0/D$ for $\lambda = 0$ (**a**), $\lambda = 1.25$ (**b**) and $\lambda = 2.5$ (**c**). Positive vorticity is *red* and negative is *blue*

contracta above the turbine due to the limited height of the channel and the blockage caused by the turbine. The wake behind the turbine shows the continued effect of the vortex pair, which mixes faster fluid above the turbine with slower fluid in the wake. For the stationary turbine (Fig. 8a), these two regions remain separate and coherent for the entire measurement region. Adding rotation and the effect of the tip vortices blurs the distinction between the two regions, and for the highest TSR (Fig. 8c), the mean velocity profile at the end of the domain shows little evidence of the turbine upstream. Figure 9 shows velocity profiles extracted at $X/D = 6.5$ along the lateral symmetry plane. The increasing uniformity of the velocity profiles is the result of quicker wake recovery with increasing TSR.

Streamwise velocity along the wall-parallel plane at the mid-height of the turbine is shown in Fig. 10. The near wake of the turbine is almost symmetric about the $Z = 0$ plane and comprises the individual wakes of turbine model components, consistent with Figs. 5 and 6. The rotation of the turbine causes a larger, connected wake region that persists up to $X/D = 2$. In this region, the increase in vortex strength with TSR causes greater wake asymmetries and velocity deficit. Further downstream, the increased entrainment of high-velocity fluid due to the stronger vortices quickens wake recovery and decreases asymmetry for higher TSR. Figure 11 substantiates the discussion above, presenting profiles of streamwise velocity extracted at $X/D = 6.5$ along the plane at $Y/D = 0.7$. The profile of the stationary turbine is nearly symmetric, while the profiles behind the rotating turbine show a very asymmetric profile at $\lambda = 2.5$, yet even more at $\lambda = 1.25$.

3.2.2 Velocity deficit

Streamwise planes (Figs. 8, 10) both show evidence of quickening wake recovery with increasing TSR. To quantify wake recovery, the velocity deficit behind the
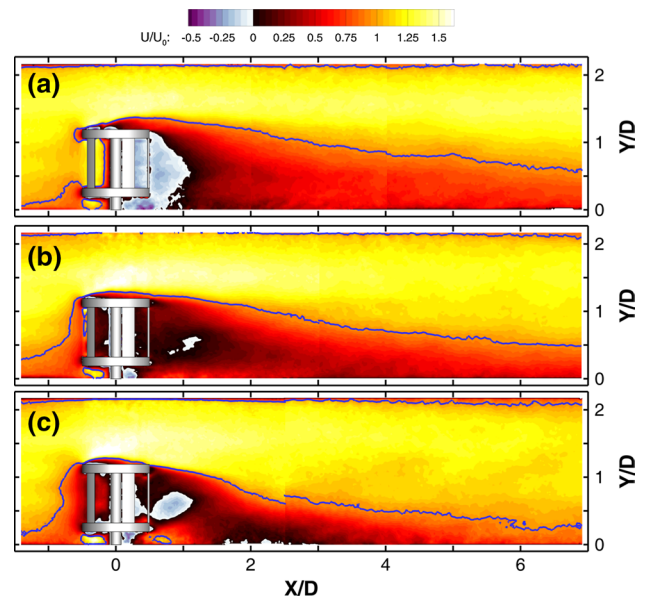

Fig. 8 *Color contours* of streamwise velocity on the lateral symmetry plane, $Z = 0$, for $\lambda = 0$ (**a**), $\lambda = 1.25$ (**b**), and $\lambda = 2.5$ (**c**). The *blue* contour indicates the location of $U/U_0 = 0.95$
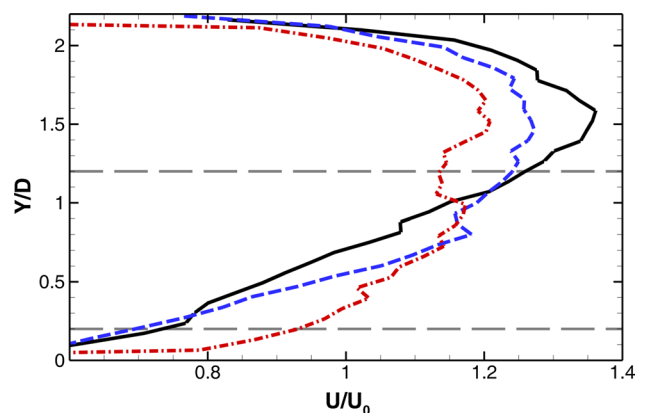

Fig. 9 Profiles of streamwise velocity along a vertical axis on the lateral symmetry plane, $Z = 0$, at $X/D = 6.5$, for $\lambda = 0$ (*solid black*), $\lambda = 1.25$ (*dashed blue*), and $\lambda = 2.5$ (*dash-dotted red*). The *horizontal lines* indicate the *bottom* and *top* of the turbine model. The profiles indicate quicker wake recovery with increasing TSR
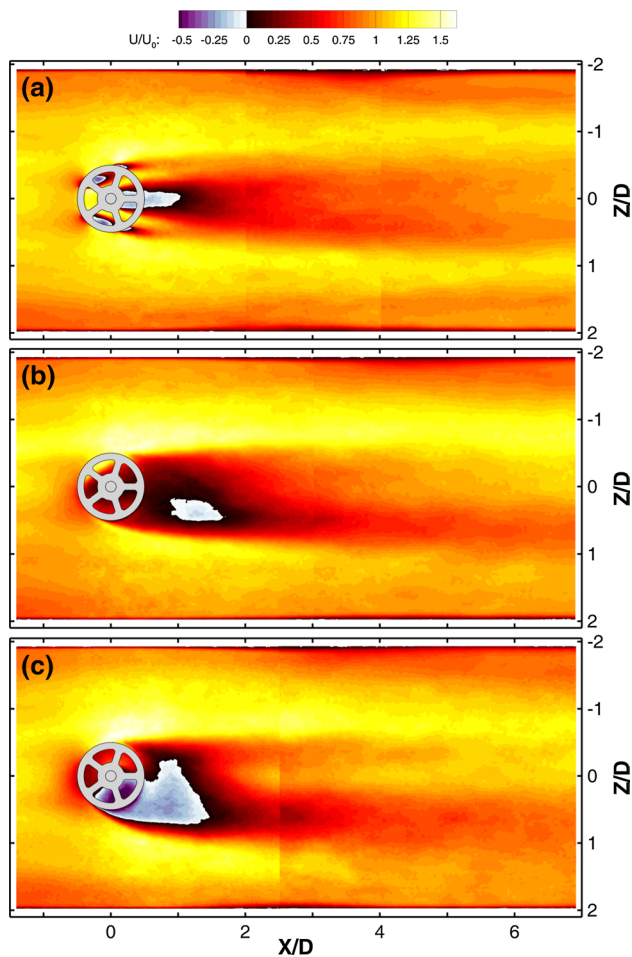
Fig. 10 *Color contours* of streamwise velocity on a wall-parallel plane at the turbine mid-height, $Y/D = 0.7$, for $\lambda = 0$ (**a**), $\lambda = 1.25$ (**b**) and $\lambda = 2.5$ (**c**)
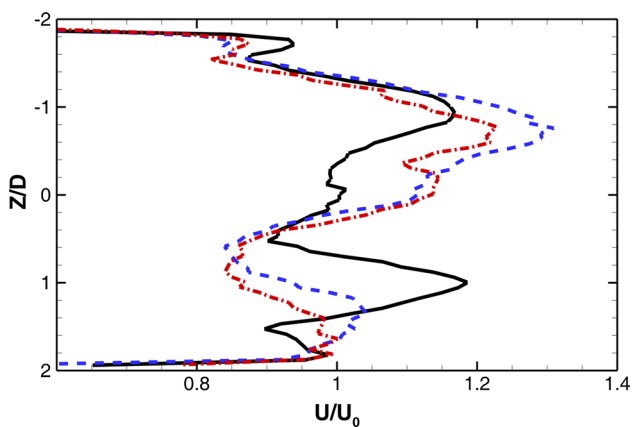

Fig. 11 Lateral profiles of streamwise velocity at turbine mid-height, $Y/D = 0.7$, at $X/D = 6.5$, for $\lambda = 0$ (*solid black*), $\lambda = 1.25$ (*dashed blue*), and $\lambda = 2.5$ (*dash-dotted red*)

turbine is calculated by averaging the streamwise velocity downstream of the turbine. The region used for velocity averaging is the projected frontal area of the turbine, $0.2 \leq Y/D \leq 1.2$, $-0.5 \leq Z/D \leq 0.5$. The volume over which the velocity deficit is evaluated is shown in Fig. 12a. This region was selected to investigate how wake recovery would affect the flow approaching a second VAWT located directly downstream of the initial turbine, as might exist in a multi-row wind farm array. Transverse planes color contoured by the streamwise velocity are displayed at several X/D locations for $\lambda = 2.5$. The streamwise velocity is averaged over the projected area and plotted as $\langle U \rangle / U_0$ in Fig. 12b as a function of streamwise location. Discontinuities in the curves result from the merging of two regions of interest for each TSR. Near the turbine ($X/D < 1$), the average velocity decreases with increasing TSR. Immediately downstream of the turbine ($X/D = 0.5$), the average velocities for $\lambda = 0$, 1.25, and 2.5 are 51, 29, and 15 % of the bulk flow velocity U_0, respectively. Despite starting with the lowest average velocity behind the turbine, the $\lambda = 2.5$ case shows the quickest recovery, surpassing the recoveries
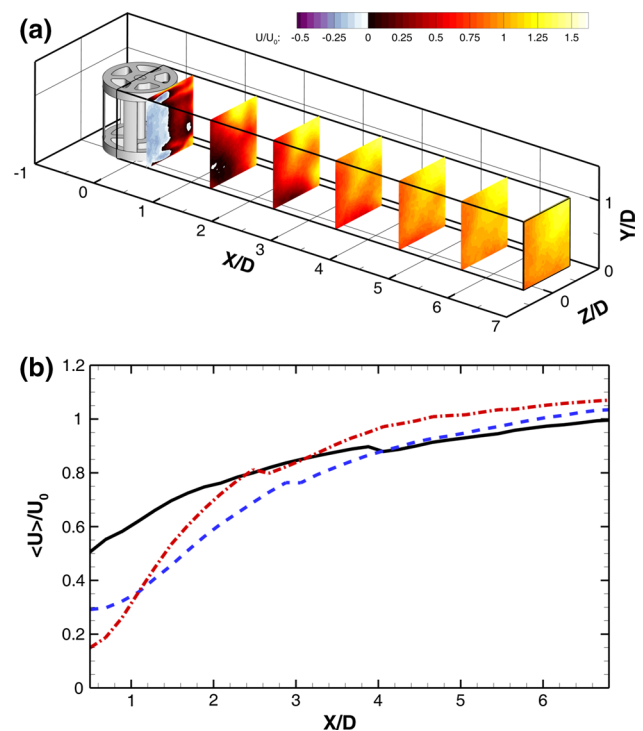

Fig. 12 Velocity deficit calculations. The volume used to calculate the velocity deficit is shown in (**a**), with several transverse slices showing *color* contours of streamwise velocity for $\lambda = 2.5$. Streamwise velocities are averaged over each of these slices to create streamwise-varying velocity deficits for each TSR, (**b**) $\lambda = 0$ (*solid black*), $\lambda = 1.25$ (*dashed blue*) and $\lambda = 2.5$ (*dash-dotted red*)

of $\lambda = 1.25$ at $X/D = 1.1$ and $\lambda = 0$ at $X/D = 3.1$. At $X/D = 3.9$ the average velocity behind the turbine operating at $\lambda = 2.5$ has recovered to 95 % of U_0, matching the findings of Dabiri (2011). The $\lambda = 1.25$ case has the next quickest wake recovery, exceeding the recovery of the stationary turbine at $X/D = 4.1$ and reaching 95 % of U_0 at $X/D = 5.0$. The stationary turbine has the slowest recovery, with the average velocity returning to 95 % of U_0 at $X/D = 5.5$.

The increase of vortex strength with TSR has a two-fold effect on the velocity deficit. First, stronger vortices mix more high-velocity fluid from the freestream into the low-velocity wake. Additionally, the $\lambda = 2.5$ case shows stronger lateral velocity in the common flow between vortices (Fig. 6f) than the $\lambda = 1.25$ case. The stronger lateral velocity shifts the wake from behind the turbine, increasing the wake recovery in the projected area behind the VAWT (Figs. 6f, 10c).

3.2.3 3D wake topology

The effect of the strong vortices shown in Fig. 6 is visualized through a stream-surface constructed from the measured velocity field. A series of streamlines are started on a contour that is the projection of the turbine onto an transverse slice located at the most upstream location of the measurement domain, $X/D = -1.4$. Due to greater uncertainty in streamline calculations near the walls of the channel, only streamlines for which $Y/D \geq 0.35$ are considered. Individual streamlines are combined into a stream-surface, which by definition is impenetrable by the mean flow. The stream-surface roughly represents the boundary between the fluid that passes through the turbine and the freestream fluid that is deflected around it. Two views of the stream-surface constructed for the $\lambda = 2.5$ case are shown in Fig. 13. Figure 13a shows the blockage effect as the stream-surface expands in the vicinity of the turbine. As a consequence of the finite tunnel cross-section and the impermeability of the stream-surface to mean velocity, the flow on the exterior of the stream-surface must accelerate as the stream-surface area increases, causing the higher velocity regions seen in Fig. 6. Further downstream, the effect of the dominant vortex originating from the top, upwind-turning side of the turbine can be seen in the distortion of the stream-surface. The higher velocity fluid on the exterior of the stream-surface is entrained within the wake behind the turbine, as visible in the end view in Fig. 13b.

The stream-surface provides a convenient way to measure the blockage effect caused by the turbine and its wake.
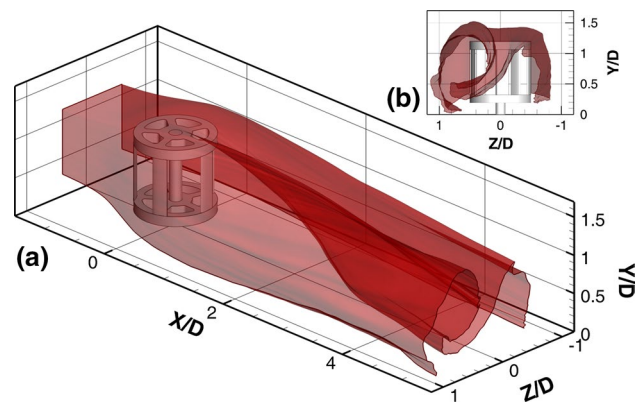

Fig. 13 3D isometric (**a**) and end (**b**) views of stream-surface for $\lambda = 2.5$. The effect of the tip vortex on the distortion of the wake is clear
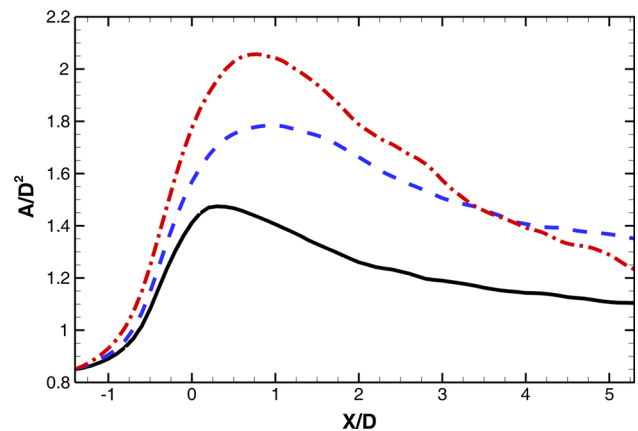

Fig. 14 Area enclosed by the stream-surface as function of streamwise position for $\lambda = 0$ (*solid black*), $\lambda = 1.25$ (*dashed blue*), and $\lambda = 2.5$ (*dash-dotted red*)

Cross-sections of the stream-surface at different streamwise positions are considered, and the area of the cross-sections is calculated from the extracted profiles. The open ends of the cross-sections at the bottom of the stream-surface are connected to create a closed contour. The area enclosed by the stream-surface reflects the amount of blockage seen by the incoming flow. Stream-surface areas for all three TSRs are shown in Fig. 14.

At the center of the turbine, $X/D = 0$, there is already a significant augmentation of the blockage above the projected area of the turbine. The maximum stream-surface area for each TSR occurs shortly after the center of the turbine. For the rotating turbines, the maximum blockage is found further downstream, indicating that the wake behind the spinning turbine continues to provide a significant blockage beyond the physical turbine rotor. The value

of the maximum blockage increases with increasing TSR. The stream-surface cross-section area for $\lambda = 2.5$ decreases more rapidly than for $\lambda = 1.25$, reaching a smaller area at $X/D = 3.5$. This rapid decrease is the result of the stronger entrainment into the wake for $\lambda = 2.5$.

3.2.4 Velocity triangles

The blades of VAWTs see a periodically changing incoming flow as they rotate, experiencing phases of lift and stall depending on their velocity relative to the local flow. Knowing the local fluid velocity is critical to identifying regions where aerodynamic behaviors such as stall might occur. For the two rotating turbine cases, the local mean flow in the vicinity of the blades is examined through the velocity triangles defined by: (1) the absolute flow velocity, (2) the blade velocity, and (3) the flow velocity relative to the moving blade. The velocity field in the middle 40 % of the turbine height ($0.5 \leq Y/D \leq 0.9$) is largely two-dimensional in the XZ plane, with minimal variation of the streamwise and lateral components in the wall-normal direction. The velocity field is averaged over this height to create a two-dimensional, two-component mean velocity field representative of that seen by the blades. While phase-locked measurements of local velocity in the vicinity of the blades would be optimal for this analysis, the present measurements of the time-averaged velocity field comprise the most complete experimental data for the three-dimensional flow field in the vicinity of the turbine blades. The use of the time-averaged velocity field is a significant improvement over the use of unperturbed bulk flow velocity to construct velocity vectors, as is previously described in Dixon et al. (2008) and Laneville and Vittecoq (1986). From this 2D field, the local velocity vectors are determined as a function of the azimuthal location, θ, defined in Fig. 2.

As seen in Fig. 4, the flow on the interior and exterior surfaces of the blades can differ drastically, especially along the upwind-turning side of the turbine. To create a single local velocity representative of the flow seen by a turbine blade, vectors are averaged within a circular area at each azimuthal location. Circles are centered at a radial coordinate of $R/D = 0.482$, the distance from the rotor axis to the blade center. The robustness of this approach was tested by using circles of different diameter D_c. Figure 15a shows the averaging areas at $\theta = 45°$ for $\lambda = 1.25$. The streamwise and lateral velocity components resulting from the area averaging are shown in Fig. 15b, c for $\lambda = 1.25$. The components of the averaged velocity are largely independent of the size of the averaging area (also for $\lambda = 2.5$, not shown). All subsequent analyses will use velocities
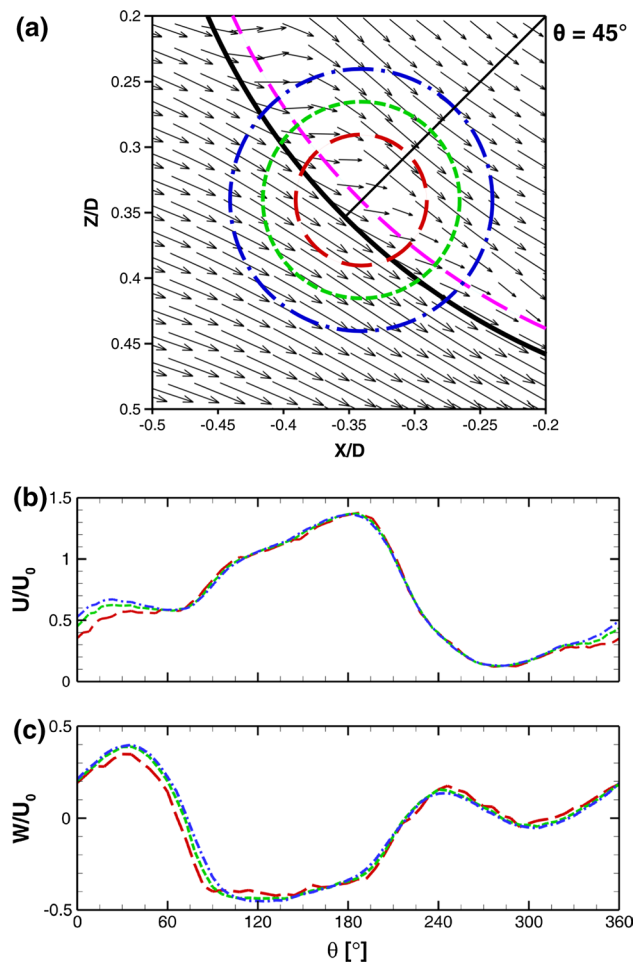

Fig. 15 Averaged velocity field for $\lambda = 1.25$ at $\theta = 45°$. **a** The *solid black line* is the outer edge of the turbine; the magenta line is the location of the blade centers, $R/D = 0.482$. The diameters of the circles are $D_c = 0.5C$ (*dashed red*), $0.75C$ (*dotted green*), and C (*dash-dotted blue*), where C is the chord length of the blade. Variation in mean velocity components (**b**, **c**) as function of azimuthal position. The *color* and pattern of the *lines* match the circles in (**a**)

obtained using the largest diameter circle, $D_c = C$, where C is the blade chord length.

Velocity triangles are constructed using the area averaged local fluid velocity, the known rotation rate of the turbine, Ω, and the blade position. The fluid velocity relative to the moving blade is found by the difference of these two velocity vectors. Triangles at eight azimuthal locations are shown in Fig. 16 for the two rotating turbines. The direction and magnitude of the local fluid velocity vary significantly between the two TSRs. On the upwind-turning side of the turbine, the faster rotation rate at $\lambda = 2.5$ causes a reversal in the direction of the local fluid velocity with respect to the $\lambda = 1.25$ case.
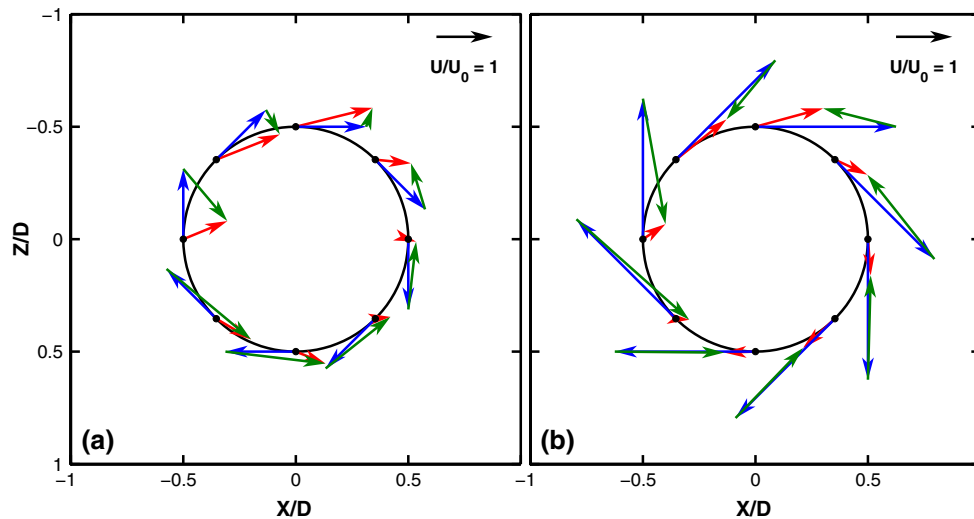
Fig. 16 Velocity triangles for $\lambda = 1.25$ (**a**) and $\lambda = 2.5$ (**b**). *Triangles* are constructed from the local fluid velocity (*red*), velocity of the turbine blade (*blue*), and relative velocity of the fluid with respect to the moving turbine blade (*green*)

3.2.5 Angle of attack

The velocity triangles of Fig. 16 are used to determine a turbine blade's angle of attack (AOA) as a function of θ. For this analysis, AOA is defined in Fig. 17.

AOAs for the two TSRs are shown as a function of azimuthal coordinate in Fig. 18. In addition to the curves extracted from the data, an idealized AOA is shown for each experimental TSR as a dashed line. This idealized curve was found by assuming that the local fluid velocity at each blade is entirely in the streamwise direction with $U/U_0 = 1$. Additional idealized curves are also shown for other TSRs for the purposes of comparison. While this is a naïve model of the local flow around a rotating turbine, it is a reasonable *a priori* assumption and is often used to describe turbine behavior [e.g., by Dixon et al. (2008) and Laneville and Vittecoq (1986)].

The measured angles of attack for both TSRs differ significantly from the theoretical curves. For the $\lambda = 1.25$ case, there is a jump in angle of attack from $-180°$ to $180°$ at $\theta = 160°$. This indicates that, at this location,

the local fluid velocity is moving faster than the blades, despite the greater than unity TSR. Fluid deflected around the turbine is accelerated by a *vena contracta*, creating the local increase in velocity. For $0° < \theta < 90°$ and $210° < \theta < 360°$, the measured angle of attack is less than the theoretical value and lies under a magnitude of $10°$ for much of this region. The same occurs for the higher TSR, with measured angles of attack under $5°$ in magnitude for $0° < \theta < 55°$ and $250° < \theta < 360°$. This region maps to the upwind-turning side of the turbine, where the blade motion is the dominant factor in determining the relative fluid velocity (see Fig. 16). The curves for both TSRs have large angles of attack at $\theta = 180°$, where the theoretical model predicts AOA $= 0°$. At this location, the blades are turning directly downstream, but due to the deflection of flow around the turbine, the actual local velocity has a lateral component. For $\lambda = 2.5$, the measured AOA range is much smaller than in the theoretical model for $\lambda = 2.5$ and is closer to the theoretical range for $\lambda = 4$. A smaller angle of attack could lead to less stall on turbine blades than anticipated by using the theoretical curves.
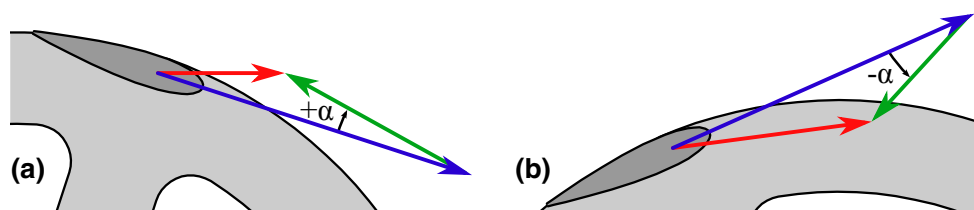

Fig. 17 Definition of positive (**a**) and negative (**b**) AOA, showing local velocity vector (*red*), turbine blade velocity (*blue*), and fluid velocity relative to moving blade (*green*). A positive AOA occurs

when the relative velocity passes across the blade traveling outward from the center of the turbine
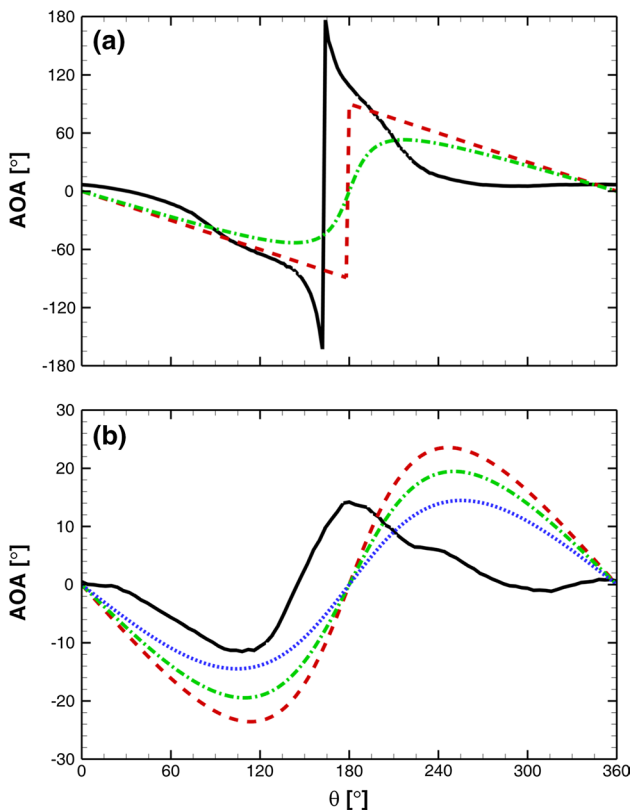
Fig. 18 Measured and ideal angles of attack for $\lambda = 1.25$ (**a**) and $\lambda = 2.5$ (**b**). Measured AOAs are shown in *solid black lines*. In (**a**), the idealized curves are shown for $\lambda = 1$ (*dashed red*) and $\lambda = 1.25$ (*dash-dotted green*). In **b**, the idealized curves are shown for $\lambda = 2.5$ (*dashed red*), $\lambda = 3$ (*dash-dotted green*), and $\lambda = 4$ (*dotted blue*). Note the change in vertical scaling between (**a**) and (**b**)

4 Conclusions

Three-dimensional mean flow field measurements around and downstream of a VAWT at TSRs of 0, 1.25, and 2.5 provide new information for choosing the layout and spacing of dense turbine arrays. A vortex pair, formed at the upwind-turning side of the turbine, is shown to increase in strength with TSR and strongly influences wake development. Near the rotor, the higher TSR causes a more asymmetric wake with stronger velocity deficit. A large reverse flow region forms in the near wake, extending on both sides of the turbine axis. However, further downstream the stronger vortex pair in the high TSR case entrains high momentum fluid into the wake. It follows that the vortex strength, and therefore the wake recovery, is enhanced with increasing TSR. If one limits the analysis to the mean flow, higher TSRs are beneficial for the sake of minimizing aerodynamic interference between VAWTs by reducing the extent of an individual turbine's wake.

The second focus of this paper is the description of flow in the vicinity of the turbine rotor, which is strongly influenced by rotation. The availability of measurements both inside and outside the rotor allows a unique evaluation of the varying mean flow environment around the turbine blades through the rotation cycle. The flow within the turbine largely follows the rotation of the solid rotor, while the flow outside the rotor is highly distorted by its presence. The flow induced by the rotation changes the local velocity at various blade positions from the unperturbed incoming velocity that is often used in blade element analysis. Velocity triangles constructed from locally averaged velocity fields provide the blade angle of attack for the rotating cases. The measured angles of attack show significant differences with respect to idealized curves that assume an unperturbed flow velocity. For the slower spinning turbine, the measured angle of attack is less than the idealized curve for most azimuthal positions, but also shows behavior indicative of a turbine operating at or less than a TSR of unity. For the faster turbine, the measured angle of attack shows magnitudes more similar to the idealized case at $\lambda = 4$.

The present analysis is strictly valid only for the specific turbine geometry studied. Further research is warranted that explores, for example, the effect of the aspect ratio. In general, the present study indicates that the three-dimensional description of the flow is critical for characterizing the wake of a VAWT. The measurements presented in this paper represent the time-averaged flow field around a spinning turbine model. To understand the unsteady behavior caused by the periodic passing of the blades, future work will include phase-locked MRV measurements.

We remark that in full-scale VAWTs applications the Reynolds number is up to two orders of magnitudes higher than in the present measurements. Although in this fully separated flow the vorticity transport dynamics are likely to be qualitatively similar, the quantitative features are expected to depend on the Reynolds number regime. Therefore, investigations at full scale are needed in order to corroborate our conclusions.

The design of space-efficient wind farms of vertical axis wind turbines requires the use of accurate computational models. State-of-the-art models of VAWTs use the actuator line method (ALM) to simulate turbine blades rotating in a flow field, but at present there is a lack of high-resolution, three-dimensional, three-component velocity measurements needed to evaluate such models. The present study provides data against which models such as the actuator line model can be validated. The three-dimensional nature of the turbine wake exposed by the present study calls into question numerical simulations of the wake performed in 2D. Although such simulations would not be able to

capture the full wake behavior *a priori*, they may be necessary to reduce the cost of the simulation of an entire wind farm. As such, the results of the present study can be used to improve 2D models of the wake development. To be further applicable to the optimization of VAWT arrays in a wind farm, future work will focus on the interaction of wakes of two turbines.

References

Araya D, Dabiri J (2015) A comparison of wake measurements in motor-driven and flow-driven turbine experiments. Exp Fluids 56(7):150

Bachant P, Wosnik M (2014) Reynolds number dependence of cross-flow turbine performance and near-wake characteristics. In: 2nd marine energy technology symposium

Battisti L, Zanne L, Dell'Anna S, Dossena V, Persico G, Paradiso B (2011) Aerodynamic measurements on a vertical axis wind turbine in a large scale wind tunnel. ASME J Energy Resour Technol 133(3):031201

Bazilevs Y, Korobenko A, Deng X, Yan J, Kinzel M, Dabiri J (2014) Fluid–structure interaction modeling of vertical-axis wind turbines. J Appl Mech 81(8):081,006

Brochier G, Fraunie P, Beguier C, Paraschivoiu I (1986) Water channel experiments of dynamic stall on darrieus wind turbine blades. J Propuls Power 2(5):445–449

Castelli MR, Englaro A, Benini E (2011) The darrieus wind turbine: proposal for a new performance prediction model based on cfd. Energy 36(8):4919–4934

Coletti F, Elkins C, Eaton J (2013) An inclined jet in crossflow under the effect of streamwise pressure gradients. Exp Fluids 54(9):1–16

Dabiri J (2011) Potential order-of-magnitude enhancement of wind farm power density via counter-rotating vertical-axis wind turbine arrays. J Renew Sustain Energy 3(4):043104

Dixon K, Simão Ferreira C, Hofemann C, van Bussel G, van Kuik G (2008) A 3d unsteady panel method for vertical axis wind turbines. In: The proceedings of the European wind energy conference and exhibition Brussels

Dossena V, Persico G, Paradiso B, Battisti L, Dell'Anna S, Brighenti A, Benini E (2015) An experimental study of the aerodynamics and performance of a vertical axis wind turbine in a confined and unconfined environment. J Energy Resour Technol 137(5):051,207

Elkins C, Markl M, Pelc N, Eaton J (2003) 4d magnetic resonance velocimetry for mean velocity measurements in complex turbulent flows. Exp Fluids 34(4):494–503

Ferreira C, van Kuik G, van Bussel G (2006) Wind tunnel hotwire measurements, flow visualization and thrust measurement of a vawt in skew. In: 44th AIAA aerospace sciences meeting and exhibit, American Institute of Aeronautics and Astronautics

Ferreira C, Hofemann C, Dixon K, van Kuik G, van Bussel G (2010) 3-d wake dynamics of the vawt: Experimental and numerical investigation. In: 48th AIAA aerospace sciences meeting including the new horizons forum and aerospace exposition, American Institute of Aeronautics and Astronautics

Fortunato B, Dadone A, Trifoni V (1995) A two-dimensional methodology to predict vertical axis wind turbine performance. J Solar Energy Eng 117(3):187–193

Hau E (2005) Wind turbines: fundamentals, technologies, application, economics. Springer, Berlin

Hofemann C, Simão Ferreira C, Dixon K, van Bussel G, van Kuik G, Scarano F (2008) 3d stereo piv study of tip vortex evolution on a vawt. In: EWEC 2008-European wind energy conference—Brussels

Howell R, Qin N, Edwards J, Durrani N (2010) Wind tunnel and numerical study of a small vertical axis wind turbine. Renew Energy 35(2):412–422

Kinzel M, Mulligan Q, Dabiri J (2012) Energy exchange in an array of vertical-axis wind turbines. J Turbul 13(38):1–13

Laneville A, Vittecoq P (1986) Dynamic stall: the case of the vertical axis wind turbine. J Solar Energy Eng 108(2):140–145

McTavish S, Feszty D, Nitzsche F (2014) An experimental and computational assessment of blockage effects on wind turbine wake development. Wind Energy 17(10):1515–1529

Pelc N, Sommer F, Li K, Brosnan T, Herfkens R, Enzmann D (1994) Quantitative magnetic resonance flow imaging. Magn Reson Q 10(3):125–147

Raciti Castelli M, De Betta S, Benini E (2012) Effect of blade number on a straight-bladed vertical-axis darreius wind turbine. World Acad Sci Eng Technol 61:305–311

Rajagopalan R, Fanucci J (1985) Finite difference model for vertical axis wind turbines. J Propuls Power 1(6):432–436

Rolin V, Porté-Agel F (2015) Wind-tunnel study of the wake behind a vertical axis wind turbine in a boundary layer flow using stereoscopic particle image velocimetry. In: Journal of physics: conference series, vol 625. IOP Publishing, p 012012

Roy S, Saha UK (2014) An adapted blockage factor correlation approach in wind tunnel experiments of a savonius-style wind turbine. Energy Conv Manag 86:418–427

Shamsoddin S, Porté-Agel F (2014) Large eddy simulation of vertical axis wind turbine wakes. Energies 7(2):890–912

Sørensen B (2004) Renewable energy: its physics, engineering, environmental impacts, economics & planning. Elsevier, London

Whittlesey R, Liska S, Dabiri J (2010) Fish schooling as a basis for vertical axis wind turbine farm design. Bioinspir Biomim 5(3):035,005